Fluoride Clusterfullerenes: Tuning Metal-Metal Bonding and Magnetic Properties Via Single Fluorine Atom Doping

Yi Shen,[#] Yannick Roselló,[#] Laura Abella,[#] Jiawei Qiu,[#] Xiya Du, Qingyu Meng, Lihao Zheng, Zhengkai Cao, Zhiwen He, Josep M. Poblet, Luis Echegoyen, Lei Sun, Antonio Rodríguez-Fortea,[*] Ning Chen[*]

KEYWORDS: Actinide, Fullerene, metal-metal bonding, Qubit

ABSTRACT: Endohedral fullerenes are known for their exceptional ability to host metal clusters which contain unique bonding motifs. In this study, we report a facile strategy to synthesize a new family of clusterfullerenes, the fluoride clusterfullerenes (FCFs). This work demonstrates that actinides and rare earth metals as well as alkaline earth metals can be encapsulated within a variety of fullerene cages and these fullerenes can be obtained in their pristine form without additional functionalization methods. Notably, $Th_2F@I_h(7)$-C_{80} and $CaScF@C_s(6)$-C_{82}, were isolated and their molecular structures and magnetic properties were characterized by X-ray single-crystal diffraction and multiple spectroscopic techniques, as well as DFT calculations. These findings reveal that the unique internal addition of a single fluorine atom significantly alters the metal-metal bonding interaction of Th-Th and Ca-Sc. While $Th_2@I_h(7)$-C_{80} hosts a σ^2 Th-Th bond, an unprecedented Actinide-Actinide (Th-Th) single electron metal-metal bond is formed inside $Th_2F@I_h(7)$-C_{80}, upon the internal addition of fluoride. Similarly, while Ca-Sc single electron bond exists in $CaSc@C_s(6)$-C_{82}, which exhibits excellent molecular qubit properties, the addition of fluoride transforms the compound into a singlet. The present study not only highlights the successful synthesis of a novel family of fluoride clusterfullerenes, which will likely be an extensive family, it also shows that fluorine doping can induce novel metal-metal bonding motifs leading to potentially intriguing magnetic properties.

INTRODUCTION

Understanding the basic concepts of chemical bonding is essential in the field of chemistry, as it forms the basis for predicting chemical reactions and conducting further synthetic procedures. One type of bonding interaction is the metal-metal bond, which involves a direct interaction between metal atoms.[1-3] This type of bonding has significant implications in catalysis, metallic surface chemistry, and magnetism, and it underlies a wide range of phenomena in both natural and synthetic systems.[4-7] While metal-metal bonds between transition metals have been intensively investigated in recent years,[8-10] metal-metal bonds involving lanthanides and actinides, which have limited valence 4f and 5f orbitals, remain as a challenge.[11-13]

Interestingly, fullerenes, with their hollow internal space, can function as unique nano-containers and encapsulate metal ions.[14-15] Due to its unique nano-scale confined space and electron transfer as well as coordination interactions between the embedded metal ions and the carbon cages, fullerenes provide an ideal environment for the formation of elusive metal-metal bonds.[16-17] Novel metal-metal bonds involving lanthanides and actinides have been successfully stabilized by the encapsulation of metal ion pairs into the fullerene cages. Single-electron bonds, such as in $ThY@C_{78}$,[18] $LaTi@C_{82}$,[19] $Y_2@C_{79}N$,[20] $Dy_2@C_{80}(CH_2Ph)$[21] and two-electron bonds, such as in $Th_2@C_{80}$,[22] $U_2@C_{80}$,[23-24] and $ScY@C_{82}$[25], have been successfully characterized. Most of these novel metal-metal interactions have not been obtained in other kinds of compounds, which highlight the unique value to study metal-metal interactions inside fullerenes. These findings have also enlightened researchers in the organometallic compounds, which contain similar metal-metal bonds and exhibit unique molecular magnetism, have been successfully synthesized in the recent studies.[11, 26-27]

On the other hand, fullerene cages can also capture electronegative non-metallic elements such as C, N, O, S, etc., acting as bridging ligands between two metals.[15] Very recently, Shi and coworkers reported the synthesis and characterization of fluoride clusterfullerene derivatives.[28] In their study, polytetrafluoroethylene (PTFE) was used as a fluorine source during the arcing process and $M_2F@C_{80}$ (M=Gd, Y) were extracted with DMF to afford monoanions $[M_2F@C_{80}]^-$; afterwards, by electrophilic trifluoromethylation $M_2F@C_{80}(CF_3)$ compounds were finally obtained. This method, however, like the previously reported $M_2@C_{2n}(CF_3)$, requires a CF_3 addition on the fullerene cage to stabilize the compound. Fluorine, as the most electronegative element, can lead to highly localized electronic density in fluorides, enabling strong binding with "hard" (i.e., highly charged, weakly polarizable) metal ions.[29] However, how the internal doping of fluoride affects the chemical and physical properties of these clusterfullerenes remains unexplored.

In this work, we present a facile strategy for the synthesis of a series of novel fluoride clusterfullerenes (FCFs). By using metal fluorides as metal and fluorine sources, a family of pristine fluoride clusterfullerenes, which encapsulated rare earth metals and alkaline earth metals, as well as two actinide metals, were successfully synthesized and characterized for the first time. Particularly, different from the recent report, these novel endohedral fullerene compounds are stable in their pristine form, with no additional functionalization. Moreover, combined experimental and theoretical studies were employed to investigate the molecular structures, the encapsulated bonding motifs as well as the magnetic properties (EPR). The results

show that the unique internal addition of a single fluorine atom alters the metal-metal bonding interaction of Th-Th and Ca-Sc. In particular, an unprecedented Actinide-Actinide (Th-Th) single electron metal-metal bond is formed with the addition of fluoride. In addition, with the number of unpaired electrons (open/closed-shell character) altered by internal addition of fluorine, the molecular magnetic properties of these compounds were also altered as compared to their dimetallofullerene analogues.

RESULTS AND DISCUSSION

Syntheses and isolation of pristine fluoride clusterfullerenes

In this work, metal fluoride powder was chosen as both the metal and fluoride sources, which facilitates the generation of the metal fluoride clusters during the arc discharging process. Utilizing this strategy, pristine FCFs, such as $Th_2F@C_{80}$ and $CaScF@C_{82}$, were synthesized by The Krätschmer–Huffman DC arc discharge method.[30] Graphite rods, packed with metal fluoride (ThF_4 for $Th_2F@C_{80}$, CaF_2/Sc_2O_3 for $CaScF@C_{82}$) and graphite powder with a molar ratio of ThF_4:C=1:30 and CaF_2:Sc_2O_3:C=1:0.5:20, were vaporized in the arcing chamber under a 200 Torr He atmosphere. The obtained soot was then collected and extracted with CS_2 for 12 h. Multistage high-performance liquid chromatography (HPLC) procedures were employed to isolate dimetallic FCFs $Th_2F@C_{80}$ and $CaScF@C_{82}$, along with dimetallic fullerenes $Th_2@C_{80}$[22] and $CaSc@C_{82}$, as shown in Figure S1–S5. Additionally, we observed $CaSc@C_{80}$ and $CaScF@C_{80}$ during this process, but subsequent characterization was limited due to their relatively low abundance. The variety of both encapsulated metal fluoride clusters and the host fullerene cages show that this synthetic strategy can be applied to synthesize an extensive family of fluoride clusterfullerenes. Moreover, different from the very recent report in which the FCF was extracted in an anionic form and an additional functionalization was needed to obtain the stable $M_2F@C_{80}(CF_3)$ compound,[28] this method yields stable pristine FCF compounds with no need for additional chemical functionalization.

The purity of $Th_2F@C_{80}$, $CaSc@C_{82}$ and $CaScF@C_{82}$ were confirmed by the single peaks in HPLC and sole peaks at 1442.828 m/z, 1044.739 m/z and 1063.839 m/z by MALDI-TOF mass spectrometry, and the observed isotopic distribution agrees well with the theoretical calculations (see Figure 1).

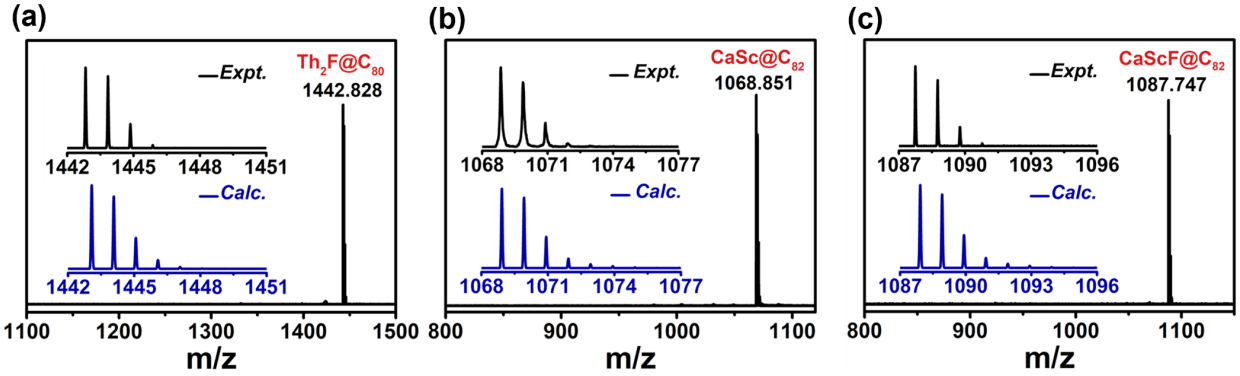

Figure 1. The positive-ion mode MALDI-TOF mass spectra of (a) $Th_2F@C_{80}$, (b) $CaSc@C_{82}$ and (c) $CaScF@C_{82}$. The insets show the expansions of the corresponding experimental isotopic distributions in comparison with the theoretical ones.

Actinide metal FCF $Th_2F@C_{80}$ and Th-Th single electron bond

Molecular structure of $Th_2F@I_h(7)$-C_{80}·[Ni^{II}(OEP)].

The black block cocrystal was obtained by the slow diffusion of a Ni^{II}(OEP) (OEP = 2, 3, 7, 8, 12, 13, 17, 18-octaethylporphyrin dianion) solution in benzene into a CS_2 solution of the corresponding EMF. The molecular structure of the obtained crystal was determined by single-crystal X-ray diffraction analysis and refined as $Th_2F@I_h(7)$-C_{80}·[Ni^{II}(OEP)] $2C_6H_6$ (OEP = 2, 3, 7, 8, 12, 13, 17, 18-octaethylporphyrin dianion) in the monoclinic *C*2/*m* (No. 12) space group. Figure 2a shows that $Th_2F@I_h(7)$-C_{80} co-crystallized with one Ni^{II}(OEP) molecule, due to substantial π–π interaction between them. In the compound, Ni^{II}(OEP) is responsible for hindering the rotation of the fullerene cage and facilitates structure determination.[31]

For clarity, only one orientation of the fullerene cage together with the major site of the Th_2F cluster are shown in Figure 2, while the other disordered sites and occupancies of internal atoms are shown in Figure S6a and Table S2. The two dominant Th atoms are located over two non-parallel hexagons in the $I_h(7)$-C_{80}, as shown in Figure 2b. Notably, the two Th atoms are no longer situated on the same C_2 axis of $I_h(7)$-C_{80}, in contrast to the Th atoms within $Th_2@I_h(7)$-C_{80}.[22] With the introduction of the single F atom, one of the inner metal atoms shifts to a position under an adjacent hexagon and deviates from the original C_2 axis. The distances between the Th atoms and the closest cage carbons range from 2.330(16) to 2.623(29) Å, with Th1 and Th2 at distances to their corresponding hexagon centroids of 2.010(2) and 2.029(3) Å, respectively, similar to those observed for $Th_2@I_h(7)$-C_{80}. It indicates a strong interaction between the Th metals and the fullerene cage in $Th_2F@I_h(7)$-C_{80} analogous to that in $Th_2@I_h(7)$-C_{80}.[22] The experimental Th-Th distance of 3.651(3) Å is notably shorter than that observed in $Th_2@I_h(7)$-C_{80} (3.816(6) Å), consistent with the theoretically calculated distances. It is evident that incorporation of the F atom inside the limited space of the C_{80} cage causes a new binding motif and results in a small Th-F-Th angle of 99.87° and a shorter Th-Th distance. The Th-F distances for the Th_2F cluster are 2.357(14) Å and 2.414(15) Å, comparable to Th-F bond lengths for previously reported thorium fluorides: 2.307(2) to 2.374(6) Å for $[(Th_2F_5)(NC_7H_5O_4)_2(H_2O)][NO_3]$,[32] 2.418(7) Å to 2.634(7) Å for ThO_4F_5 polyhedra,[33] and average value 2.379 Å for Hexagonal $CsTh_3F_{13}$.[34] These results are consistent with theoretical calculations which show that Th-F bonds are ionic.

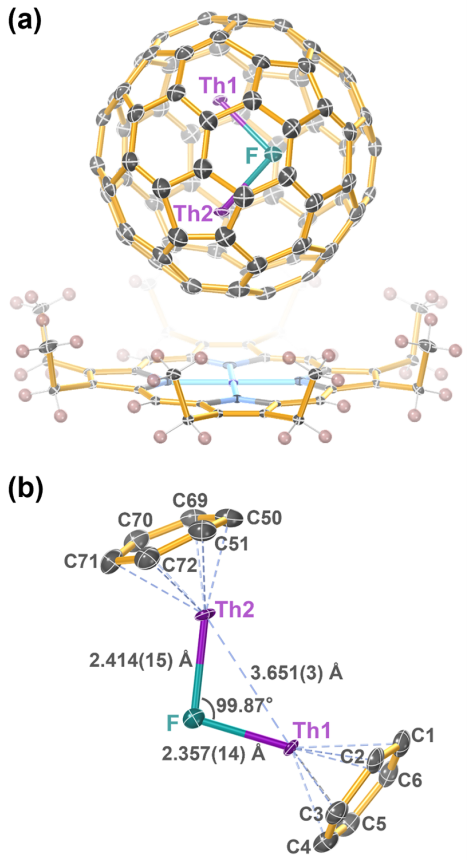

Figure 2. (a) ORTEP drawing of $Th_2F@I_h(7)$-C_{80}·[Ni^{II}OEP] with 10% thermal ellipsoids. Only one cage orientation and the selected Th (Th1 with 0.334 occupancy and Th2 with 0.254 occupancy) sites are shown, and the solvent molecules are omitted for clarity. (b) Fragment view of the relationship between the inner Th/F/Th unit and the closest cage segments.

Computational study of electronic structure and bonding in $Th_2F@C_{80}$.

To describe the electronic structure of $Th_2F@I_h(7)$-C_{80} we can assume that there is a formal transfer of six electrons from the actinide fluoride cluster to the cage, $[Th_2F]^{6+}@C_{80}^{6-}$, as usually occurs for EMFs with the $I_h(7)$-C_{80} isomer.[14, 35] We have confirmed that the fluoride clusterfullerene observed by X-ray crystallography is by far lower in energy (>100 kcal mol^{-1}) than the corresponding dimetallofullerene with an attached exohedral fluorine, $Th_2@C_{80}$-F (Figure S7), as observed in previous laser ablation experiments.[36] The optimized $Th_2F@I_h(7)$-C_{80} structure (PBE0/TZP/D3 level, see Computational Details) shows Th-F distances of 2.291 and 2.290 Å and a Th-F-Th angle of 110.3°, with a Th-Th distance of 3.760 Å, in good agreement with the experimental structure. The Th-cage distances to nearest C atoms range between 2.52-2.58 Å and are comparable to those for $Th_2@I_h(7)$-C_{80} (2.55 Å, in average). The doublet ground state shows the spin density localized on the Th_2F cluster, in particular, distributed equally on the two Th atoms. The singly-occupied molecular orbital (SOMO) is a sigma orbital delocalized between the two Th atoms (Figure 3b). Therefore, there exists a sigma single-electron Th-Th bond even with the presence of a fluoride bridging the two actinides, showing an unprecedented bond type in actinide dimers. Unfortunately, we did not obtain a CW EPR spectrum for $Th_2F@C_{80}$, which is likely due to the severe line broadening caused by the strong spin-orbit coupling of Th. The Bader's Quantum Theory of Atoms in Molecules analysis was performed to further characterize the Th-Th interaction.[37] The *bond critical point* (bcp) between two atoms, postulated by Bader, is a necessary and sufficient condition for the atoms to be bonded. The Bader analysis shows a bond critical point in between the two Th atoms, not exactly in the middle of the Th-Th axis, but slightly shifted, making a Th-bcp-Th angle of 150.3°. The values of the density and the Laplacian of the density at the bcp (ρ_{bcp} = 0.16 eÅ^{-3} and $\nabla^2\rho_{bcp}$ = -0.098 eÅ^{-5}), as well as the Th-Th delocalization index (0.343) confirm the presence of this single-electron bent or banana bond. Besides, the Th-F bonds can be described as rather ionic bonds (ρ_{bcp} = 0.54 eÅ^{-3} and $\nabla^2\rho_{bcp}$ = 7.24 eÅ^{-5}), as found for Sc-F and Ca-F bonds in $CaScF@C_s(6)$-C_{82} (see below). Interestingly, the Th-Th distance in $Th_2F@C_{80}$ is slightly shorter than in $Th_2@C_{80}$, even though the two-electron sigma Th-Th bond is stronger than the single-electron bond in Th-F-Th. This counterintuitive observation can be rationalized by considering that the main factor influencing the position and the structural characteristics of the cluster within the cage in endohedral fullerenes is the interaction between the metal atoms and the carbon cage. For the two systems, the Th-cage distances are mainly the same. However, upon fluorination, the relatively large Th-F distances (2.3-2.4 Å) force the cluster to adopt a highly bent configuration (approximately 100 degrees). This adjustment is due to the limited space inside the spherical $I_h(7)$-C_{80} cage leading to a somewhat shorter Th-Th distance in $Th_2F@C_{80}$ compared to $Th_2@C_{80}$.

Due to the synthetic challenge, the study of An-An metal-metal bond is rare. So far, we have identified three types of An-An bond, which are: (i) strong Th-Th σ^2 bond in $Th_2@C_{80}$; (ii) weak U-U σ^2 bond in $U_2@C_{80}$; and (iii) strong triple $\sigma^2\pi^4$ bond in $U_2@C_{2n}$ ($2n \leqslant 60$).[22-24] In 2021, Liddle and co-workers also reported σ-aromatic Th-Th bonding in a tri-thorium cluster.[38] Here, surprisingly, by the doping of a single F atom into the Th-Th moiety inside the fullerene cage, not only two Th-F ionic bonds are formed, but a novel An-An single electron bent bond is also present, which represents a new type of An-An metal bond.

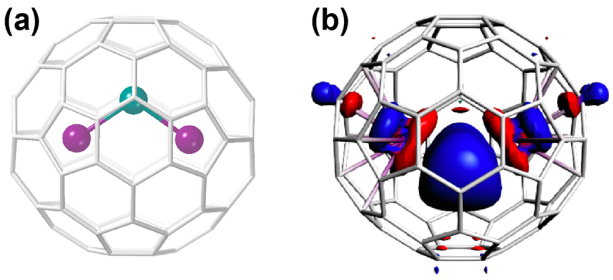

Figure 3. (a) DFT-optimized geometry of $Th_2F@I_h(7)$-C_{80}. (b) Singly-occupied molecular orbital (SOMO) of $Th_2F@I_h(7)$-C_{80}.

Alkaline earth/rare earth metal FCF $CaScF@C_s(6)$-C_{82}

Molecular structure of $CaSc@C_s(6)$-C_{82}·[Ni^{II}(OEP)] and $CaScF@C_s(6)$-C_{82}·[Ni^{II}(OEP)].

The molecular structures of $CaSc@C_s(6)$-C_{82} and $CaScF@C_s(6)$-C_{82} were unambiguously determined by single-crystal X-ray diffraction studies. Black crystal blocks of $CaSc@C_s(6)$-C_{82}·[Ni^{II}(OEP)] $2C_6H_6$ and $CaScF@C_s(6)$-C_{82}·[Ni^{II}(OEP)] $2C_6H_6$ were obtained by slow diffusion of a benzene solution of Ni^{II}(OEP) into a CS_2 solution of the samples. Figure 4a and 5a show the molecular structures of the two

previously unreported EMFs together with the cocrystallized Ni^{II}(OEP) molecules.

CaSc@C_s(6)-C_{82}. The fullerene cage of CaSc@C_s(6)-C_{82} exhibits two orientations attributed to the crystallographic mirror of the *C*2/*m* space group. As shown in Figure S6, Ca and Sc ions are highly ordered and only two sites (Ca1, Sc1 and their mirror-related counterparts Ca1A, Sc1A) are observed inside the fullerene cage. Considering the previously reported crystallographic studies of CaY@C_s(6)-C_{82},[39] we selected the Ca1 and Sc1 positions for further analysis, (see Figure 4a).

As shown in Figure 4b, the Ca ion resides in the center above a hexagon, with the closest Ca-cage contact falling within a range of 2.513(6)–2.607(6) Å, in agreement with the theoretical calculations. The Sc ion resides over the [6, 6] carbon bond (between a pair of adjacent hexagon rings) with the shortest Sc-cage distance ranging from 2.154(6)–2.162(8) Å, comparable to

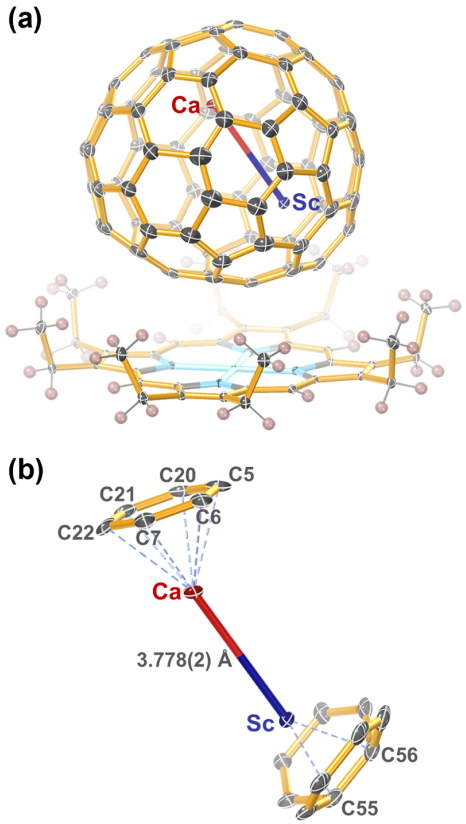

Figure 4. (a) ORTEP drawing of CaSc@C_s(6)-C_{82}·[Ni^{II}OEP] with 20% thermal ellipsoids. Only one cage orientation and the selected Ca (Ca1 with 0.5 occupancy) and Sc (Sc1 with 0.5 occupancy) sites are shown, and the solvent molecules are omitted for clarity. (b) Fragment view of the relationship between the inner Ca/Sc unit and the closest cage portion.

calculations (2.173–2.198 Å) and to the Sc-C distances in Sc_2@C_{3v}(8)-C_{82} (2.21-2.40 Å) and ScY@C_{3v}(8)-C_{82} (2.225-2.447 Å).[17, 25] The details of metal-cage distances and metal positions for CaSc@C_s(6)-C_{82} are depicted in Table S4. The distance between Ca and Sc is determined to be 3.778(2) Å, comparable to the Ca-Y distance (3.691 Å) for CaY@C_s(6)-C_{82} and Sc-Y distance (3.674 Å) for ScY@C_{3v}(8)-C_{82}.[25, 39] As for CaY@C_s(6)-C_{82} and ScY@C_{3v}(8)-C_{82}, a metal-metal bond is also present for CaSc@C_s(6)-C_{82} (see below).

CaScF@C_s(6)-C_{82}. Similar to CaSc@C_s(6)-C_{82}, the crystal of CaScF@C_s(6)-C_{82} with a *C*2/*m* space group exhibits two crystallographic mirror-related orientations with the same occupancy of 0.5. The encapsulated Ca and Sc ions shows two sites (Ca1, Sc1 and their mirror-related counterparts Ca1A, Sc1A) respectively. Additionally, the F atom situated on the crystallographic mirror plane shows exclusively one site, as shown in Figure S6c. The computational results regarding the metal positions in the fullerene cage are discussed in subsequent sections.

The interaction of the Ca-F-Sc unit and the closest cage portion is illustrated in Figure 5b. The Ca-F-Sc angle of 143.9° is much larger than the M-F-M bond angles (M=Th and Gd) in C_{80} cages. It indicates that the Ca-F-Sc cluster is flexible and stretches out in the larger inner space of the C_{82} cage. The metal sites of Ca and Sc are found to be near to those in the CaSc@C_s(6)-C_{82}.

For CaScF@C_s(6)-C_{82}, the Ca ion resides in the center over a hexagon with the closest Ca-cage contacts in the range of 2.492(8)–2.579(8) Å, as well as the Sc ion above the [6, 6] carbon bond with the shortest Sc-cage distance ranging from 2.142(8)–2.167(6) Å. Notably, upon introduction of the single F atom into the endohedral Ca-Sc moiety, the Ca-Sc distance in CaScF@C_s(6)-C_{82} stretches to 3.907(2) Å from that of the CaSc@C_s(6)-C_{82} (3.778(2) Å). This stretched distance may be caused by the transfer of a single-electron from the Ca-Sc bond and formation of a metal-fluoride ionic bond, which will be discussed below.

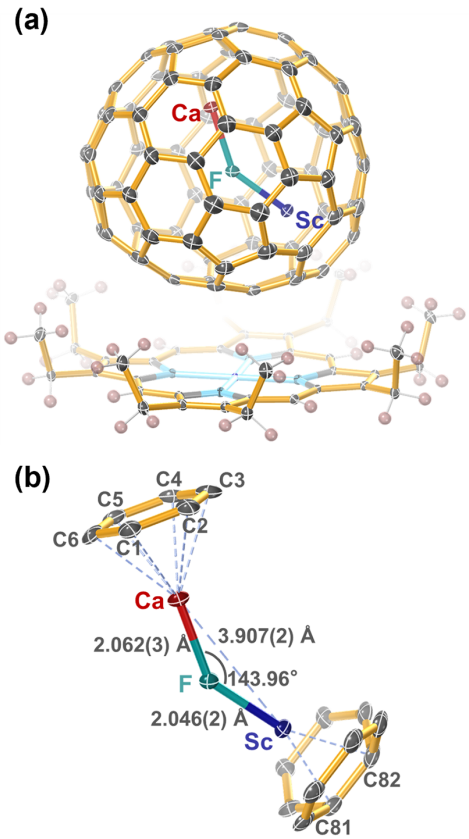

Figure 5. (a) ORTEP drawing of CaScF@C_s(6)-C_{82}·[Ni^{II}OEP] with 20% thermal ellipsoids. Only one cage orientation and the selected Ca (Ca1 with 0.5 occupancy) and Sc (Sc1 with 0.5 occupancy) sites are shown, and the solvent molecules are omitted for clarity. (b) Fragment view of the relationship between the inner Ca/F/Sc unit and the closest cage portion.

Computational study of electronic structures and Ca-Sc interactions in CaSc@C_{82} and CaScF@C_{82}.

To further understand the electronic structure and bonding nature of CaSc@C_s(6)-C_{82} and CaScF@C_s(6)-C_{82}, calculations at the PBE0/TZP/D3 level were done. Figure S9 and S10 provides the DFT-optimized geometry of CaSc@C_s(6)-C_{82}, which shows a spin-doublet ground electronic state as in CaY@C_{82}.[39] Different positions of Ca and Sc inside C_s(6)-C_{82} were explored (see Figure S11). The lowest-energy structure corresponds to the analogous metal positions of CaY@C_s(6)-C_{82}, with the Y site replaced by Sc. The DFT optimization of the crystallographic structure for Ca1 and Sc1 positions shows the lowest energy; crystallographic equivalent Ca1m and Sc1m positions lead to a structure 8.0 kcal·mol^{-1} higher in energy. When the metal positions are exchanged in CaSc@C_s(6)-C_{82} the relative energy increases to 6.6 kcal·mol^{-1}. The optimized Ca-Sc bond length is 3.771 Å, in very good agreement with experimental results. The Ca atom remains at the center of a hexagon from an s-indacene motif with the closest contacts within the range of 2.545 to 2.610 Å, similar to those Ca-cage distances in CaY@C_s(6)-C_{82} (2.490 – 2.585 Å). Sc is placed at the center of the [6,6] bond of a pyracylene fragment showing Sc-cage bond lengths of 2.173 - 2.198 Å. The position of Sc in the pyracylene motifs is in line with (i) the largest molecular orbital contribution of the LUMO+1 of neutral C_s(6)-C_{82} cage; and (ii) the most negative region of the potential electrostatic map of the C_s(6)-C_{82}^{4-} anion (Figure S12).

For CaSc@C_s(6)-C_{82}, there is a formal transfer of four electrons to the cage, $(CaSc)^{4+}@(C_{2n})^{4-}$, so there is one valence electron that remains in the internal metals. This unpaired electron is delocalized between the two metal atoms, as the spin density distribution illustrates in Figure 6, with a certain degree of polarization towards the Sc atom. Similar to the CaY EMF systems, the atomic Mulliken spin populations are 0.4 e for Ca and 0.7 e for Sc, which is importantly driven by the s-type orbitals with the s spin density populations of 16-17% for Ca and 27-28% for Sc. The unpaired electron is delocalized in a a_1 sigma-type orbital (see Figure 6c), as a consequence of a considerable overlap between the 4s4p orbitals of Ca and the 4s4p3d orbitals of Sc (see Figure 6d). For CaSc@C_s(6)-C_{82}, more 4s orbital contribution of Sc is found than that for the Y 5s orbital in CaY@C_{2n}.

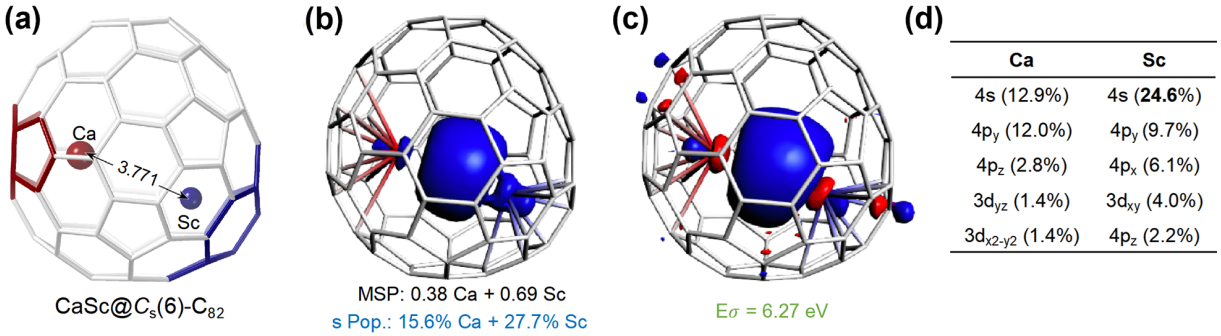

Figure 6. CaSc@C_s(6)-C_{82}: (a) DFT-optimized structure, where the Ca-Sc distance (in Å) is indicated. (b) Spin density distribution with an isosurface of ±0.002 a.u., Mulliken spin populations (MSP) and amount of s spin density population (s Pop.) of the metals. (c) Molecular orbital (MO) isosurface (±0.03 a.u.) for the delocalized sigma orbital a_1 for the alpha-spin with the corresponding MO energy (in eV). (d) Molecular orbital contributions of the σ-type bonding orbital formed essentially by n*s*, n*p* and (n-1)*d* metal orbitals.

Table 1. Computed EPR, electronic and structural parameters for different CaX@C_{2n} systems. Experimental values are in parenthesis.

	CaSc@C_{2v}(5)-C_{80}	CaSc@C_s(6)-C_{82}	CaY@C_{2v}(5)-C_{80}	CaY@C_s(6)-C_{82}	CaGd@C_{2v}(5)-C_{80}	CaDy@C_{2v}(5)-C_{80}
g-value	1.995	1.994 (2.074)	1.983 (1.982)	1.979 (1.981)	2.013	1.987
A[a]	569	603 (642)	236 (254)	245 (263)	151	447
d(Ca-X)[b]	3.919	3.773 (3.778)	3.841	3.704 (3.147)	3.830	3.850
Spin Ca[c]	0.39	0.38	0.39	0.38	0.44	0.43
Spin X[c]	0.68	0.69	0.68	0.68	7.73	5.66
S Pop.[d]	27.0	27.7	27.1	27.5	22.7	23.0
$\varepsilon_\sigma^{LUMOe}$	-3.46	-3.55	-3.50	-3.59	-3.26	-3.39
ρ_{bcp}[f]	0.077	0.086	0.091	0.100	0.093	0.090
$\nabla^2\rho_{bcp}$[f]	-0.025	-0.013	-0.063	-0.026	-0.054	-0.043
δ(Ca,X)	0.25	0.27	0.28	0.29	0.28	0.27

[a] Hyperfine coupling (in MHz). [b] Metal-metal distance (in Å). [c] Atomic Mulliken spin densities for Ca and X. [d] Amount of s spin density population on X (in %). [e] Energies of the sigma LUMO (beta) orbital (in eV). [f] Electron density and Laplacian of the electron density at the bond critical points are given in [eÅ^{-3}] and [eÅ^{-5}], respectively.

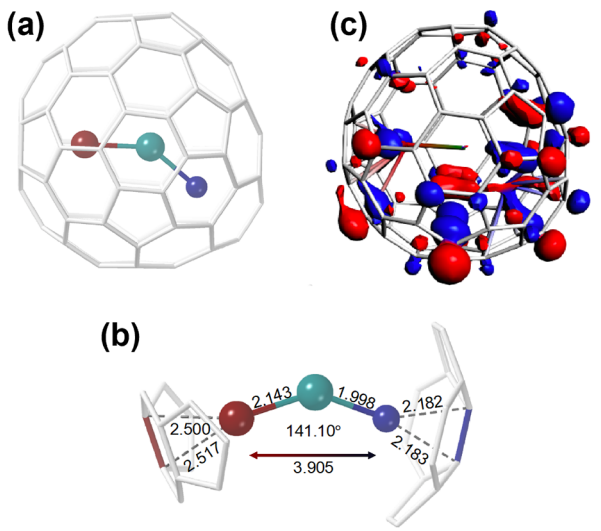

Figure 7. (a) DFT-optimized geometry of CaScF@C_s(6)-C_{82}. (b) Fragment view with the Ca-F, Sc-F, Ca···Sc and metal-cage distances (in Å) as well as the Ca-F-Sc angle. (c) Highest occupied molecular orbital (HOMO) isosurface (±0.03 a.u.).

The formal oxidation states of Ca and Sc would be near to 1.5+ and 2.5+, respectively, if they share equally the unpaired electron. The corresponding molecular orbital (MO) diagrams for the spin-doublet state of CaSc@C_s(6)-C_{82} are displayed in Figure S13. The oxidation and reduction of CaSc@C_s(6)-C_{82} are predicted to occur on the carbon cage, so the one-electron Ca-Sc σ-bond remains essentially unaltered (Figure S14).[40] The Bader's Theory analysis was performed to characterize the Ca-Sc bond. The electron density at the bcp (ρ) is 0.086 eÅ^{-3}, and the Laplacian of the electron density ($\nabla^2\rho$) is -0.013 eÅ^{-5} (see Table 1). These values indicate the presence of an accumulation of charge density in the center of the metal-metal bond. Compared to CaY@C_{2n}, lower electron density values are found for CaSc@C_{2n}, which correlates with the smaller metal-metal distances in Y-based systems.[39] The negative sign on the Laplacian is consistent with the Ca-Sc covalent interaction deduced from the singly-occupied delocalized sigma orbital.

The DFT-optimized geometry obtained from the crystallographic structure of CaScF@C_s(6)-C_{82} is displayed in Figure 7. The closed-shell singlet state is the lowest-energy electronic configuration, with the triplet spin state at 23.3 kcal·mol^{-1}. The Ca and Sc metals reside in the same positions as found in CaSc@C_{82}, and the F atom connects the two metals. The Ca-F and Sc-F bond lengths are 2.143 and 1.998 Å, respectively, and the corresponding Ca-F-Sc bond angle is 141.10º, which is smaller than that for Sc_2O@C_s(6)-C_{82} (162.2º) and larger than that for Gd_2F@C_{80}-CF_3 (116º).[28, 41] The presence of the F atom within the C_{82} cage causes the increase of the Ca-Sc distance (3.905 Å), closer contacts between the Ca and the carbon cage (2.500 Å - 2.555 Å) and a more central position of the Sc atom on the [6,6] bond of the pyracylene fragment (2.182 - 2.183 Å). Test calculations have been performed with the F atom attached to the carbon cage, i.e., forming an exohedrally functionalized fullerene, as observed in previous laser ablation experiments.[36] Interestingly, when the F atom is exohedrally attached to one carbon atom of the CaSc@C_s(6)-C_{82} cage, the relative energies oscillate in the range of 126-130 kcal·mol^{-1} (see Figure 7). Therefore, the F atom prefers energetically to be encapsulated inside the C_s(6)-C_{82} carbon cage to form a fluoride clusterfullerene.

The electronic structure is consistent with $(CaScF)^{4+}$@$(C_{82})^{4-}$, where four electrons from the CaScF cluster are formally transferred to the carbon cage. The frontier molecular orbitals (MOs) of CaScF@C_s(6)-C_{82} are mainly localized on the C_s(6)-C_{82} (Figures 7c and S14). Localized MO (LMO) analysis for CaScF@C_s(6)-C_{82} show the three filled 2p atomic orbitals of the F atom with small contributions from the metal atoms (Figure S15).

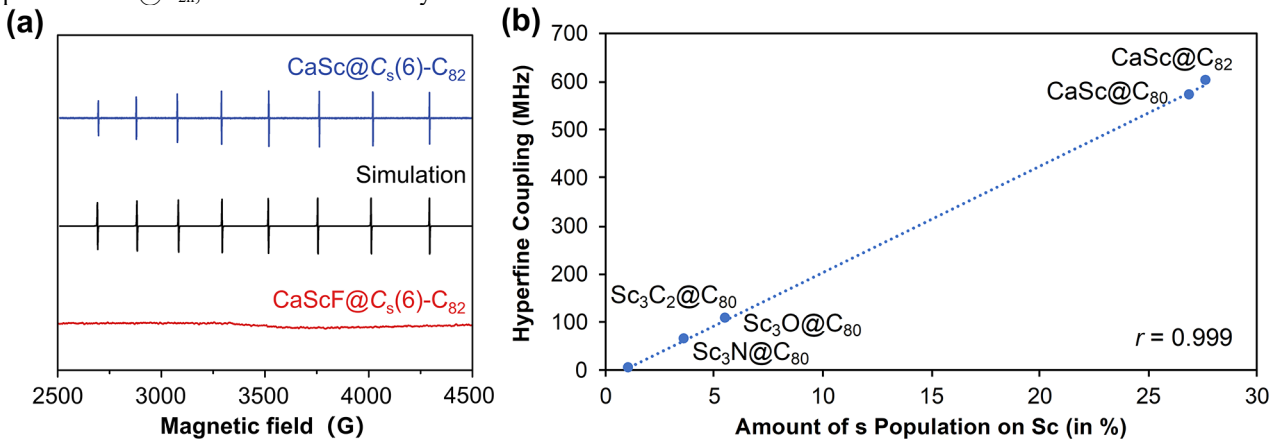

Figure 8. (a) The EPR X-band spectra of CaSc@C_s(6)-C_{82} and CaScF@C_s(6)-C_{82} measured at room temperature. The black smooth curve represents the simulated EPR spectrum of CaSc@ C_s(6)-C_{82}. (b) Correlation between the hyperfine coupling constant (in MHz) and the amount of s spin density population located on the Sc atom (in %) for CaSc@C_{2n} and Sc_3X@I_h(7)-C_{80} (X = O, N, C_2) systems. Correlation coefficient r is also given.

The Bader analysis was also performed for CaScF@C_s(6)-C_{82}, indicating the existence of bond critical points between the Ca/Sc and the F atom. The ρ_{bcp} are 0.38 and 0.55 eÅ^{-3} for Ca-F and Sc-F, respectively, and their corresponding $\nabla^2\rho_{bcp}$ present both positive signs (8.22 eÅ^{-5} for Ca-F and 11.86 eÅ^{-5} for Sc-F). Such results indicate the ionic bonding character for Ca-F and Sc-F bonds due to the high electronegativity of F. In addition, the delocalization indexes are 0.25 for Ca-F, 0.36 for Sc-F and almost nil (0.01) for Ca-Sc. Thus, different from the situation for Th_2F@I_h(7)-C_{80}, in which F doping changes the Th-Th σ^2 bond to a single electron metal-metal bond, the incorporation of the encapsulated fluoride breaks the Ca-Sc sigma bond found

in CaSc@C_s(6)-C_{82}, and results in a rather ionic metal-fluoride bonding interaction.

EPR analysis of CaSc@C_{82} and CaScF@C_{82}.

Continuous-wave (CW) EPR spectra of CaSc@C_{82} and CaScF@C_{82} were measured for CS_2 solutions to further enhance the understanding of their electronic structures. As shown in Figure 8a, eight transitions are clearly identified for CaSc@C_{82}, which are attributed to the hyperfine interactions between the electronic spin and a nuclear spin I=7/2 ^{45}Sc (100 % natural abundance), while the nuclear spin of ^{40}Ca is 0 in natural abundance 96.941 %. In addition, the diverse intensities of eight EPR peaks indicate the slightly paramagnetic anisotropy for CaSc@C_{82}, similar to that observed in other EMFs, such as Sc@C_{84},[42] CaY@C_{82},[39] TiLa@C_{82}[19] and Y_2@C_{79}N.[43] It can be attributed to substantial molecular weight and complex geometric structure for EMFs, leading to incomplete motional averaging.

The black smooth curve represents the simulated EPR spectrum of CaSc@C_s(6)-C_{82}, from which the anisotropic g tensor of $g_\perp/g_\parallel$=1.997:1.995 and hyperfine coupling constant (hfcc) tensor of $A_\perp/A_\parallel$=645:640 MHz were determined. The relatively large A values indicate strong hyperfine interactions within the bimetallic EMFs, which indicates that the unpaired electron is localized between the Ca and Sc metal ions,[19-20] and not on the carbon cage, as is the case for Sc@C_{82} (A=10 MHz). In addition, the g values of CaSc@C_{82} is comparable to those of CaY@C_{80} (g=1.9817) and CaY@C_{82} (g=1.9809).[39] All together, these results provide a direct proof that a single-electron Ca-Sc metal-metal bond is formed, consistent with the DFT calculated results.

A computational study involving other Ca-X@C_{2n} families was performed to further explore the electronic structure and the EPR parameters for CaSc@C_{2n} systems. Besides the previously reported systems CaY@C_{2v}(5)-C_{80} and CaY@C_s(6)-C_{82}, we have worked with CaSc@C_{2v}(5)-C_{80} and hypothetical Ca-X@C_{2v}(5)-C_{80} (X = Gd, Dy) systems. The calculated *g* values for CaSc@C_{2v}(5)-C_{80} and CaSc@C_s(6)-C_{82} are 1.995 and 1.994, respectively, and the calculated hfcc are 569 MHz for CaSc@C_{2v}(5)-C_{80} and 603 MHz for CaSc@C_s(6)-C_{82}. The spin density located on the Sc atom is the same for both CaSc@C_{2n} cages (0.68-0.69 e), similar to Y in the CaY@C_{2n} systems (0.68 e). CaSc@C_s(6)-C_{82} shows the largest hfcc among all the systems studied herein. The slightly larger amount of s spin density population located on Sc (27.7 *vs.* 27.0%) correlates with the larger hfcc of CaSc@C_s(6)-C_{82}, compared to that of CaSc@C_{2v}(5)-C_{80}. In addition, both CaSc@C_{2n} systems also show the largest hfcc among other Sc_3X@C_{2v}(5)-C_{80} (X = O, N, C_2) endohedral fullerenes.[14, 44] Interestingly, the hfcc and the amount of s population on the Sc atom displays a very good correlation (see Figure 8b). All the CaX systems show a spin density on Ca that is smaller than 0.5e, ranging from 0.38 to 0.44e, in line with the presence of a polarized sigma bond. The bond parameters from the Bader analysis are also comparable, with similar densities at the bond critical points, Ca-X delocalization indices and small and negative values of the Laplacian of the electron density (Table 1).

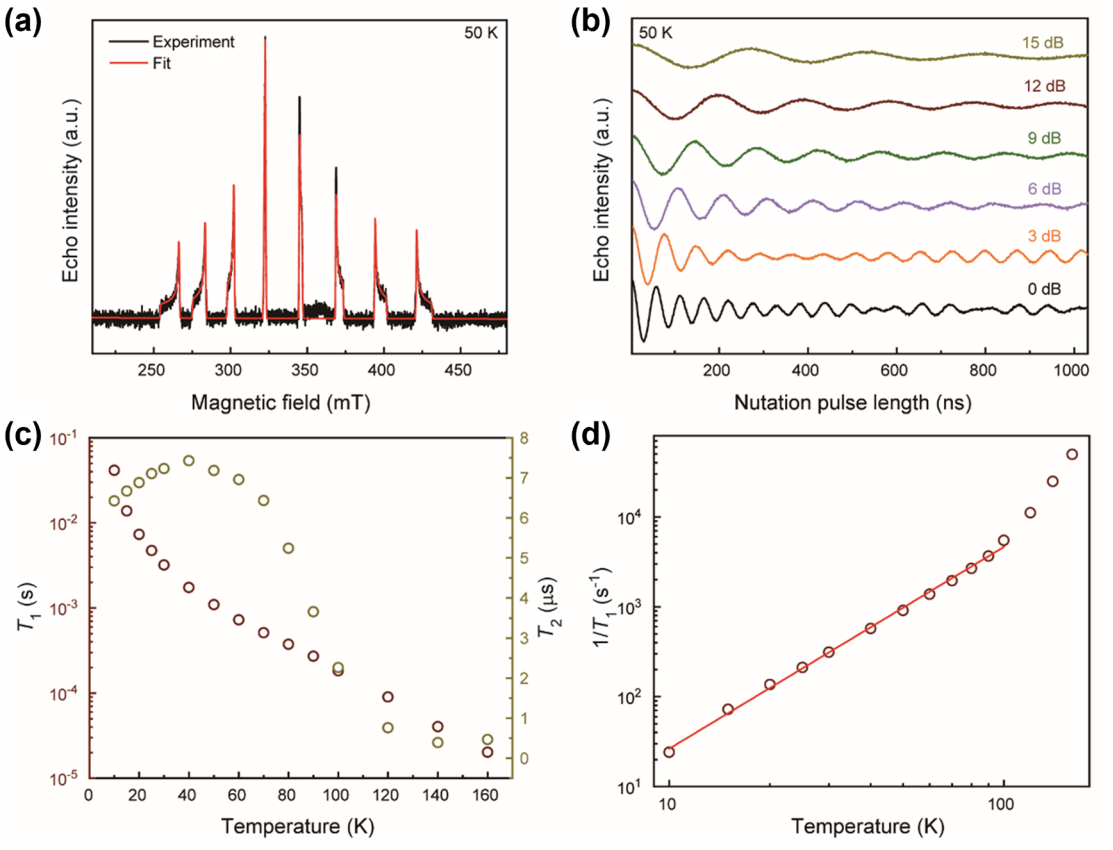

Figure 9. The X-band pulse EPR characterization of CaSc@C_s(6)-C_{82} dissolved in toluene. (a) EDFS spectrum at 50 K. (b) Rabi oscillations under various microwave attenuations at 50 K. (c) Temperature dependence of T_1 and T_2. (d) Temperature dependence of $1/T_1$. The red line is a fit with the Raman relaxation process.

To explore the potential applications of CaSc@C_s(6)-C_{82} in quantum information science,[45-47] we dissolved it in toluene and employed X-band (9.6 GHz) pulsed EPR spectroscopy to characterize its qubit behavior. The echo-detected field sweep (EDFS) spectrum obtained at 50 K clearly reveals anisotropic g-factors and a hyperfine splitting with ^{45}Sc (I = 7/2, 100% natural abundance) (Figure 9a). It was fitted with S = 1/2, $g_{\parallel}$ = 2.00066(10), $g_{\perp}$= 1.99201(5), $A_{\parallel}$ = 707.7(4) MHz, and $A_{\perp}$ = 614.7(1) MHz. The hyperfine splitting constants are significantly larger than those of CaY@C_s(6)-C_{82},[39] indicating higher electron spin distribution on the s-orbitals of Sc. Nutation experiments performed at 322.6 mT revealed Rabi oscillations at various microwave powers (Figure 9b and Figure S16), demonstrating the coherent addressability of CaSc@C_s(6)-C_{82}.

We further conducted spin dynamic studies with CaSc@C_s(6)-C_{82} to determine its spin-lattice relaxation time (T_1) and spin decoherence time (T_2), two key metrics of electron spin qubits (Figure S17 and Table S6). The T_1 and T_2 values are comparable for all hyperfine sublevels at 50 K (Figure S18), so we focused on the transition at 322.6 mT that shows the highest EDFS intensity. Thanks to its s-orbital character, the Ca-Sc single electron spin maintains quantum coherence up to 160 K (Figure 9c), close to the melting point of toluene (T_{melt} = 178.2 K).[48] Because of the weaker spin-orbit coupling of Sc than Y, the T_1 of CaSc@C_s(6)-C_{82} is significantly longer than that of CaY@C_s(6)-C_{82} from 10 – 160 K, reaching 41.5 ms at 10 K, that is more than 5 times the latter (Figure S19).[39] Below 100 K, the spin-lattice relaxation is dominated by the Raman process with $\frac{1}{T_1} \propto T^{2.24}$, indicating a low Debye temperature (Figure 9d).[45] The T_1 deviates from this trend above the glass transition temperature of toluene (T_{glass} = 113 K) as a result of the solvent disturbance. The values of T_2 and its temperature dependence are consistent with those of CaY@C_s(6)-C_{82}, likely because of similar nuclear spin environments involving ^{1}H and ^{13}C in toluene and ^{13}C in the C_{82} cage (Figure S19). The detuned rotation of the methyl group of toluene causes an increase of T_2 with rising temperature, which reaches a maximum of 7.43 μs at 40 K. Above 40 K, the T_2 decreases with rising temperature, manifesting the influence of spin-lattice relaxation on the coherence, and it tends to level off between T_{glass} and T_{melt} of toluene. Overall, CaSc@C_s(6)-C_{82} behaves as an electron spin qubit with better spin dynamic properties than CaY@C_s(6)-C_{82}.

Finally, analysis of the EPR spectrum for CaScF@C_s(6)-C_{82} shows no signal (Figure 8a). Clearly, the doping of the single F atom between Ca and Sc altered the bonding between them and quenched the spin of the Ca-Sc single electron bond, obtaining in this case an electronic closed-shell system. The lack of EPR activity for CaScF@C_s(6)-C_{82} is in agreement with the electronic structure obtained by DFT computations.

CONCLUSIONS

In this work, we present the facile synthesis of a new series of pristine clusterfullerenes, i.e., actinide metal FCF, alkaline earth/rare earth metal FCF. We successfully isolated and characterized two notable examples: Th_2F@I_h(7)-C_{80} and CaScF@C_s(6)-C_{82}. Our results reveal that, in addition to the potential variety of metals and oxidation states that can be encapsulated inside the fullerenes as fluoride clusters, the metal-metal bonding interaction as well as the magnetic properties of these compounds can be fine-tuned by the internal doping of a single fluorine atom. For example, Th_2@C_{80} exhibits a closed-shell ground state featuring a two-electron sigma Th-Th bond. However, upon the internal incorporation of a fluorine atom, one electron is removed from the Th-Th bond leading to the formation of an unprecedented single electron Th-Th bond. The electronic structure of the encapsulated Th_2F cluster is determined to be $(Th^{3.5+}F^-Th^{3.5+})^{6+}$, indicating that the formal oxidation state of Th ions is +3.5. Similarly, CaSc@C_s(6)-C_{82} possesses a single electron in a sigma Ca-Sc bonding orbital, which confers excellent molecular qubit properties. The addition of fluorine removes this electron, thus transforming the ground state of CaScF@C_s(6)-C_{82} to a singlet. Fluoride clusterfullerenes could represent an extensive and novel family of endohedral fullerenes. The fine-tuning effects achieved by the internal doping with single fluorine atoms could lead to the discovery of more unique bonding motifs and various potential applications in future studies.

ASSOCIATED CONTENT

Supporting Information.
HPLC profiles for the separation of Th_2F@I_h(7)-C_{80}, CaSc@C_s(6)-C_{82}, and CaScF@C_s(6)-C_{82}; experimental details; additional single-crystal structural parameters of the three EMFs; and complementary results from computation and pulse-EPR studies. This material is available free of charge via the Internet at http://pubs.acs.org.

Accession Codes
CCDC 2388911, 2388913, 2388914 contain the supplementary crystallographic data for this paper. These data can be obtained free of charge via www.ccdc.cam.ac.uk/data_request/cif, or by emailing data_request@ccdc.cam.ac.uk, or by contacting The Cambridge Crystallographic Data Centre, 12 Union Road, Cambridge CB2 1EZ, UK; fax: +44 1223 336033.

AUTHOR INFORMATION

Corresponding Authors

Ning Chen – College of Chemistry, Chemical Engineering and Materials Science, and State Key Laboratory of Radiation Medicine and Protection, Soochow University, Suzhou, Jiangsu 215123, P.R. China. E-mail: chenning@suda.edu.cn

Antonio Rodríguez-Fortea – Departament de Química Física i Inorgànica. Universitat Rovira i Virgili, Marcel·lí Domingo 1, 43007 Tarragona, Spain; E-mail: antonio.rodriguezf@urv.cat

Authors

Yi Shen – College of Chemistry, Chemical Engineering and Materials Science, and State Key Laboratory of Radiation Medicine and Protection, Soochow University, Suzhou, Jiangsu 215123, P.R. China

Yannick Roselló – Departament de Química Física i Inorgànica. Universitat Rovira i Virgili, Marcel·lí Domingo 1, 43007 Tarragona, Spain

Laura Abella – Departament de Química Física i Inorgànica. Universitat Rovira i Virgili, Marcel·lí Domingo 1, 43007 Tarragona, Spain

Jiawei Qiu – College of Chemistry, Chemical Engineering and Materials Science, and State Key Laboratory of Radiation Medicine and Protection, Soochow University, Suzhou, Jiangsu 215123, P.R. China

Xiya Du – Department of Chemistry, School of Science and Research Center for Industries of the Future, Westlake University, Hangzhou, Zhejiang Province 310030, China; Institute of Natural Sciences, Westlake Institute for Advanced Study, Hangzhou, Zhejiang Province 310024, China

Qingyu Meng – College of Chemistry, Chemical Engineering and Materials Science, and State Key Laboratory of Radiation Medicine and Protection, Soochow University, Suzhou, Jiangsu 215123, P.R. China

Lihao Zheng – College of Chemistry, Chemical Engineering and Materials Science, and State Key Laboratory of Radiation Medicine and Protection, Soochow University, Suzhou, Jiangsu 215123, P.R. China

Zhengkai Cao – College of Chemistry, Chemical Engineering and Materials Science, and State Key Laboratory of Radiation Medicine and Protection, Soochow University, Suzhou, Jiangsu 215123, P.R. China

Zhiwen He – College of Chemistry, Chemical Engineering and Materials Science, and State Key Laboratory of Radiation Medicine and Protection, Soochow University, Suzhou, Jiangsu 215123, P.R. China

Josep M. Poblet – Departament de Química Física i Inorgànica. Universitat Rovira i Virgili, Marcel·lí Domingo 1, 43007 Tarragona, Spain

Luis Echegoyen – Department of Chemistry, University of Texas at El Paso, El Paso, Texas 79968, United States; Institut Català d'Investigació Química, 43007 Tarragona, Catalonia, Spain

Lei Sun – Department of Chemistry, School of Science and Research Center for Industries of the Future, Westlake University, Hangzhou, Zhejiang Province 310030, China; Institute of Natural Sciences, Westlake Institute for Advanced Study, Hangzhou, Zhejiang Province 310024, China; Key Laboratory for Quantum Materials of Zhejiang Province, Department of Physics, School of Science, Westlake University, Hangzhou, Zhejiang Province 310030, China; E-mail: sunlei@westlake.edu.cn

Author Contributions

[#]Yi Shen, Yannick Roselló, Laura Abella and Jiawei Qiu contributed equally to this work.

Funding Sources

NSFC No. 52172051, KYCX24_3301, grant PID2023-149905NB-I00, grant 2021 SGR 00110, NSFC No. 22273078, TD2022004

Notes

The authors declare no competing financial interests.

ACKNOWLEDGMENT

We thank Prof. Bing-Wu Wang and Dr. Rong Sun for their assistance with EPR simulation and analysis. N. C. and Y. S. thank the National Natural Science Foundation of China (NSFC No. 52172051), the Priority Academic Program Development of Jiangsu Higher Education Institutions (PAPD) and Postgraduate Research & Practice Innovation Program of Jiangsu Province (KYCX24_3301). A.R.-F. and J.M.P. thank the Spanish Ministry of Science (grant PID2023-149905NB-I00), the Generalitat de Catalunya (grant 2021 SGR 00110) and the URV for support. X.D. and L.S. acknowledges support from the National Natural Science Foundation of China (NSFC No. 22273078) and Hangzhou Municipal Funding, Team of Innovation (TD2022004) and thank the Instrumentation and Service Center for Molecular Sciences at Westlake University for the support with the pulse EPR measurements.

REFERENCES

(1) Boronski, J. T.; Crumpton, A. E.; Wales, L. L.; Aldridge, S., Diberyllocene, a stable compound of Be(I) with a Be–Be bond. *Science* **2023**, 380 (6650), 1147-1149.

(2) Green, S. P.; Jones, C.; Stasch, A., Stable Magnesium(I) Compounds with Mg-Mg Bonds. *Science* **2007**, 318 (5857), 1754-1757.

(3) Resa, I.; Carmona, E.; Gutierrez-Puebla, E.; Monge, A., Decamethyldizincocene, a Stable Compound of Zn(I) with a Zn-Zn Bond. *Science* **2004**, 305 (5687), 1136-1138.

(4) Chipman, J. A.; Berry, J. F., Paramagnetic Metal–Metal Bonded Heterometallic Complexes. *Chem. Rev.* **2020**, 120 (5), 2409-2447.

(5) Buchwalter, P.; Rosé, J.; Braunstein, P., Multimetallic Catalysis Based on Heterometallic Complexes and Clusters. *Chem. Rev.* **2014**, 115 (1), 28-126.

(6) Cotton, F. A.; Murillo, C. A.; Walton, R. A., Multiple bonds between metal atoms. *Springer Science & Business Media:* **2006**.

(7) Shan, J.; Ye, C.; Jiang, Y.; Jaroniec, M.; Zheng, Y.; Qiao, S.-Z., Metal-metal interactions in correlated single-atom catalysts. *Sci. Adv.* 8 (17), eabo0762.

(8) Broere, D. L. J.; Modder, D. K.; Blokker, E.; Siegler, M. A.; van der Vlugt, J. I., Metal–Metal Interactions in Heterobimetallic Complexes with Dinucleating Redox‐Active Ligands. *Angew. Chem. Int. Ed*. **2016**, 55 (7), 2406-2410.

(9) Bäumer, N.; Kartha, K. K.; Buss, S.; Maisuls, I.; Palakkal, J. P.; Strassert, C. A.; Fernández, G., Tuning energy landscapes and metal–metal interactions in supramolecular polymers regulated by coordination geometry. *Chem. Sci.* **2021**, 12 (14), 5236-5245.

(10) Wang, Q.; Brooks, S. H.; Liu, T.; Tomson, N. C., Tuning metal–metal interactions for cooperative small molecule activation. *Chem. Commun.* **2021**, 57 (23), 2839-2853.

(11) Du, J.; Dollberg, K.; Seed, J. A.; Wooles, A. J.; von Hänisch, C.; Liddle, S. T., Thorium(iv)–antimony complexes exhibiting single, double, and triple polar covalent metal–metal bonds. *Nat. Chem.* **2024**, 16 (5), 780-790.

(12) Lussier, D. J.; Ito, E.; McClain, K. R.; Smith, P. W.; Kwon, H.; Rutkauskaite, R.; Harvey, B. G.; Shuh, D. K.; Long, J. R., Metal-Halide Covalency, Exchange Coupling, and Slow Magnetic Relaxation in Triangular $(Cp^{iPr5})_3U_3X_6$ (X = Cl, Br, I) Clusters. *J. Am. Chem. Soc.* **2024**, 146 (31), 21280-21295.

(13) Liddle, S. T., Molecular metal-metal bonds: compounds, synthesis, properties. *John Wiley & Sons:* **2015**.

(14) Popov, A. A.; Yang, S.; Dunsch, L., Endohedral Fullerenes. *Chem. Rev.* **2013**, 113 (8), 5989-6113.

(15) Yang, S.; Wei, T.; Jin, F., When metal clusters meet carbon cages: endohedral clusterfullerenes. *Chem. Soc. Rev.* **2017**, 46 (16), 5005-5058.

(16) Liu, F.; Velkos, G.; Krylov, D. S.; Spree, L.; Zalibera, M.; Ray, R.; Samoylova, N. A.; Chen, C.-H.; Rosenkranz, M.; Schiemenz, S.; Ziegs, F.; Nenkov, K.; Kostanyan, A.; Greber, T.; Wolter, A. U. B.; Richter, M.; Büchner, B.; Avdoshenko, S. M.; Popov, A. A., Air-stable redox-active nanomagnets with lanthanide spins radical-bridged by a metal–metal bond. *Nat. Commun.* **2019**, 10 (1).

(17) Yao, Y.-R.; Shi, X.-M.; Zheng, S.-Y.; Chen, Z.-C.; Xie, S.-Y.; Huang, R.-B.; Zheng, L.-S., Atomically Precise Insights into Metal–Metal Bonds Using Comparable Endo-Units of Sc_2 and Sc_2C_2. *CCS Chemistry* **2021**, 3 (12), 294-302.

(18) Yan, Y.; Abella, L.; Sun, R.; Fang, Y.-H.; Roselló, Y.; Shen, Y.; Jin, M.; Rodríguez-Fortea, A.; de Graaf, C.; Meng, Q.; Yao, Y.-R.; Echegoyen, L.; Wang, B.-W.; Gao, S.; Poblet, J. M.; Chen, N., Actinide-lanthanide single electron metal-metal bond formed in mixed-valence di-metallofullerenes. *Nat. Commun.* **2023**, 14 (1).

(19) Xiang, W.; Hu, Z.; Xin, J.; Jin, H.; Jiang, Z.; Han, X.; Chen, M.; Yao, Y.-R.; Yang, S., Steering Single-Electron Metal–Metal Bonds and Hyperfine Coupling between a Transition Metal-Lanthanide Heteronuclear Bimetal Confined in Carbon Cages. *J. Am. Chem. Soc.* **2023**, 145 (41), 22599-22608.

(20) Zuo, T.; Xu, L.; Beavers, C. M.; Olmstead, M. M.; Fu, W.; Crawford, T. D.; Balch, A. L.; Dorn, H. C., $M_2@C_{79}N$ (M = Y, Tb): Isolation and Characterization of Stable Endohedral Metallofullerenes Exhibiting M−M Bonding Interactions inside Aza[80]fullerene Cages. *J. Am. Chem. Soc.* **2008**, 130 (39), 12992-12997.

(21) Liu, F.; Krylov, D. S.; Spree, L.; Avdoshenko, S. M.; Samoylova, N. A.; Rosenkranz, M.; Kostanyan, A.; Greber, T.; Wolter, A. U. B.; Büchner, B.; Popov, A. A., Single molecule magnet with an unpaired electron trapped between two lanthanide ions inside a fullerene. *Nat. Commun.* **2017**, 8 (1).

(22) Zhuang, J.; Morales-Martínez, R.; Zhang, J.; Wang, Y.; Yao, Y.-R.; Pei, C.; Rodríguez-Fortea, A.; Wang, S.; Echegoyen, L.; de Graaf, C.; Poblet, J. M.; Chen, N., Characterization of a strong covalent Th^{3+}–Th^{3+} bond inside an $I_h(7)$-C_{80} fullerene cage. *Nat. Commun.* **2021**, 12 (1).

(23) Zhang, X.; Wang, Y.; Morales-Martínez, R.; Zhong, J.; de Graaf, C.; Rodríguez-Fortea, A.; Poblet, J. M.; Echegoyen, L.; Feng, L.; Chen, N., $U_2@I_h(7)$-C_{80}: Crystallographic Characterization of a Long-Sought Dimetallic Actinide Endohedral Fullerene. *J. Am. Chem. Soc.* **2018**, 140 (11), 3907-3915.

(24) Moreno-Vicente, A.; Roselló, Y.; Chen, N.; Echegoyen, L.; Dunk, P. W.; Rodríguez-Fortea, A.; de Graaf, C.; Poblet, J. M., Are U–U Bonds Inside Fullerenes Really Unwilling Bonds? *J. Am. Chem. Soc.* **2023**, 145 (12), 6710-6718.

(25) Zheng, L.; Roselló, Y.; Yan, Y.; Yao, Y. R.; Fan, X.; Poblet, J. M.; Rodríguez‐Fortea, A.; Chen, N., $ScY@C_{3v}(8)$‐C_{82}: Metal-Metal σ^2 Bond in Mixed Rare-Earth Di-metallofullerenes†. *Chin. J. Chem.* **2023**, 41 (15), 1809-1814.

(26) Sheng, W.; Rajeshkumar, T.; Zhao, Y.; Maron, L.; Zhu, C., Electronic Delocalization and σ-Aromaticity in Heterometallic Cluster with Multiple Thorium–Palladium Bonds. *J. Am. Chem. Soc.* **2024**, 146 (18), 12790-12798.

(27) Wedal, J. C.; Anderson-Sanchez, L. M.; Dumas, M. T.; Gould, C. A.; Beltran-Leiva, M. J.; Celis-Barros, C.; Paez-Hernandez, D.; Ziller, J. W.; Long, J. R.; Evans, W. J., Synthesis and Crystallographic Characterization of a Reduced Bimetallic Yttrium ansa-Metallocene Hydride Complex, $[K(crypt)][(\mu\text{-}Cp^{An})Y(\mu\text{-}H)]_2$ (Cp^{An} = $Me_2Si[C_5H_3(SiMe_3)\text{-}3]_2$), with a 3.4 Å Yttrium-Yttrium Distance. *J. Am. Chem. Soc.* **2023**, 145 (19), 10730-10742.

(28) Zhao, Y.; Hu, Z.; Chuai, P.; Jin, H.; Yang, S.; Su, J.; Shi, Z., Capturing Metal Fluoride inside a Carbon Cage. *J. Am. Chem. Soc.* **2024**, 146 (25), 17003-17008.

(29) Pedersen, K. S.; Sørensen, M. A.; Bendix, J., Fluoride-coordination chemistry in molecular and low-dimensional magnetism. *Coord. Chem. Rev.* **2015**, 299, 1-21.

(30) Krätschmer, W.; Lamb, L. D.; Fostiropoulos, K.; Huffman, D. R., Solid C_{60}: a new form of carbon. *Nature* **1990**, 347 (6291), 354-358.

(31) Olmstead, M. M.; Costa, D. A.; Maitra, K.; Noll, B. C.; Phillips, S. L.; Van Calcar, P. M.; Balch, A. L., Interaction of Curved and Flat Molecular Surfaces. The Structures of Crystalline Compounds Composed of Fullerene (C_{60}, $C_{60}O$, C_{70}, and $C_{120}O$) and Metal Octaethylporphyrin Units. *J. Am. Chem. Soc.* **1999**, 121 (30), 7090-7097.

(32) Kim, J.-Y.; Norquist, A. J.; O'Hare, D., $[(Th_2F_5)(NC_7H_5O_4)_2(H_2O)][NO_3]$: An Actinide−Organic Open Framework. *J. Am. Chem. Soc.* **2003**, 125 (42), 12688-12689.

(33) Ok, K. M.; O'Hare, D., Synthesis, structure, and characterization of a new thorium–organic framework material, $Th_3F_5[(C_{10}H_{14})(CH_2CO_2)_2]_3(NO_3)$. *Dalton Trans.* **2008**, (41), 5560-5562.

(34) Underwood, C. C.; Mann, M.; McMillen, C. D.; Kolis, J. W., Hydrothermal Descriptive Chemistry and Single Crystal Structure Determination of Cesium and Rubidium Thorium Fluorides. *Inorg. Chem.* **2011**, 50 (22), 11825-11831.

(35) Rodríguez-Fortea, A.; Balch, A. L.; Poblet, J. M., Endohedral metallofullerenes: a unique host–guest association. *Chem. Soc. Rev.* **2011**, 40 (7), 3551-3563.

(36) Moreno-Vicente, A.; Mulet-Gas, M.; Dunk, P. W.; Poblet, J. M.; Rodríguez-Fortea, A., Probing the formation of halogenated endohedral metallofullerenes: Predictions confirmed by experiments. *Carbon* **2018**, 129, 750-757.

(37) Bader, R. J. E. o. C. C., Atom in molecules a quantum theory (AIM). **1990**.

(38) Boronski, J. T.; Seed, J. A.; Hunger, D.; Woodward, A. W.; van Slageren, J.; Wooles, A. J.; Natrajan, L. S.; Kaltsoyannis, N.; Liddle, S. T., A crystalline tri-thorium cluster with sigma-aromatic metal-metal bonding. *Nature* **2021**, 598 (7879), 72-75.

(39) Qiu, J.; Abella, L.; Du, X.; Cao, Z.; He, Z.; Meng, Q.; Yan, Y.; Poblet, J. M.; Sun, L.; Rodriguez-Fortea, A.; Chen, N., $CaY@C_{2n}$: Exploring Molecular Qubits with Ca-Y Metal-Metal Bonds. *J. Am. Chem. Soc.* **2024**, 146 (35), 24310-24319.

(40) Valencia, R.; Rodríguez-Fortea, A.; Clotet, A.; de Graaf, C.; Chaur, M. N.; Echegoyen, L.; Poblet, J. M., Electronic Structure and Redox Properties of Metal Nitride Endohedral Fullerenes $M_3N@C_{2n}$ (M=Sc, Y, La, and Gd; 2n=80, 84, 88, 92, 96). *Chem. Eur. J.* **2009**, 15 (41), 10997-11009.

(41) Abella, L.; Wang, Y.; Rodríguez-Fortea, A.; Chen, N.; Poblet, J. M., Current status of oxide clusterfullerenes. *Inorg. Chim. Acta* **2017**, 468, 91-104.

(42) Inakuma, M.; Shinohara, H., Temperature-Dependent EPR Studies on Isolated Scandium Metallofullerenes: $Sc@C_{82}$(I, II) and $Sc@C_{84}$. *J. Phys. Chem. B* **2000**, 104 (32), 7595-7599.

(43) Ma, Y.; Wang, T.; Wu, J.; Feng, Y.; Jiang, L.; Shu, C.; Wang, C., Susceptible electron spin adhering to an yttrium cluster inside an azafullerene $C_{79}N$. *Chem. Commun.* **2012**, 48 (94).

(44) Abella, L.; Tang, Q.; Zhang, X.; Wang, Y.; Chen, N.; Poblet, J. M.; Rodríguez-Fortea, A., $Sc_3O@I_h(7)$-C_{80}: A Trimetallic Oxide Clusterfullerene Abundant in the Raw Soot. *J. Phys. Chem. C* **2016**, 120 (45), 26159-26167.

(45) Zhou, A.; Sun, Z.; Sun, L., Stable organic radical qubits and their applications in quantum information science. *Innovation (Camb)* **2024**, 5 (5), 100662.

(46) Brown, R. M.; Ito, Y.; Warner, J. H.; Ardavan, A.; Shinohara, H.; Briggs, G. A. D.; Morton, J. J. L., Electron spin coherence in metallofullerenes: Y, Sc, and $La@C_{82}$. *Phys. Rev. B* **2010**, 82 (3), 033410.

(47) Liu, Z.; Dong, B.-W.; Meng, H.-B.; Xu, M.-X.; Wang, T.-S.; Wang, B.-W.; Wang, C.-R.; Jiang, S.-D.; Gao, S., Qubit crossover in the endohedral fullerene $Sc_3C_2@C_{80}$. *Chem. Sci.* **2018**, 9 (2), 457-462.

(48) Ariciu, A.-M.; Woen, D. H.; Huh, D. N.; Nodaraki, L. E.; Kostopoulos, A. K.; Goodwin, C. A. P.; Chilton, N. F.; McInnes, E. J. L.; Winpenny, R. E. P.; Evans, W. J.; Tuna, F., Engineering electronic structure to prolong relaxation times in molecular qubits by minimising orbital angular momentum. *Nat. Commun.* **2019**, 10 (1), 3330.

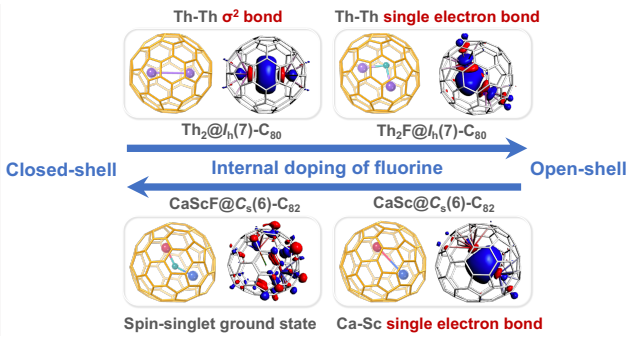
Th-Th σ² bond
Th-Th single electron bond
Th2@Ih(7)-C80
Th2F@Ih(7)-C80
Closed-shell
Internal doping of fluorine
Open-shell
CaScF@Cs(6)-C82
CaSc@Cs(6)-C82
Spin-singlet ground state
Ca-Sc single electron bond